Coastal Amplification of Tsunami Waves in The Eastern Mediterranean

EMIN ÖZSOY AND ÜMIT ÜNLÜATA

Department of Marine Science, Middle East Technical University, P.K.28, Erdemli, Icel, Turkey

MUSTAFA ARAL[1]

Department of Mathematics, Middle East Technical University, Ankara, Turkey

(Manuscript received 23 October 1980, in final form 14 November 1981)

ABSTRACT

Numerical modeling techniques are used to study tsunami propagation in the eastern Mediterranean. In addition to the propagation patterns, the amplification due to the geometries of the continental shelf and the basin are studied in detail. The surface displacement at selected strategic locations is frequency-analyzed to obtain the resonances and their modal shapes. Coupled resonances are identified in the Cilician Basin–Gulf of Iskenderun system.

1. Introduction

Historical records show that tsunamis are frequent in the Mediterranean, although they may not be as frequent as they are in the Pacific Ocean. According to Van Dorn (1965), 23 large tsunamis have occurred in the Mediterranean, while the Atlantic and Pacific Oceans have had 29 and 219 significant tsunamis respectively, throughout recorded history. Tsunamigenic events in the eastern Mediterranean have been compiled by Ambraseys (1962) in a remarkable catalogue covering the period from the second millenium B.C. to 1961. This catalogue and other seismic data bases such as those by Karnik (1969, 1971), Okamoto *et al.* (1970), Ergin *et al.* (1967) and Aslan *et al.* (1975), show that several potential source regions are located in the eastern Mediterranean. Seismotectonics of statistically relevant source regions and historical information on tsunamis from these sources have been evaluated in a previous study hereafter referred to as TSI (1979). One of the important tsunamigenic sources lies to the south of the Crete–Rhodes arc, near the western extremity of the eastern Mediterranean (Levantine) Basin. In the present paper, a tsunami event in this region is simulated. The propagation of the tsunami in the eastern Mediterranean Basin is studied to obtain the frequency response of stations along the coasts. The response is analyzed further to identify resonance mechanisms.

2. Modeling of the source region

The ground movement is modeled within a rectangular generation region of width b_0 and length l_0. The maximum ground displacement Δ_0 is assumed to occur along the centerline and to decay in the transverse direction as

$$\Delta = \Delta_0 \exp(-12|x|/b_0), \tag{1}$$

so that over a distance $|x| = b_0/4$, 95% decay occurs in the ground movement. In the lengthwise direction of the rectangular region, the ground motion is uniform. This model is in accordance with the elastic theory of Reid (1910), and has been verified in the field by Benioff (1964). The model is selected because it is simpler than the elliptical generation region of Momoi (1962) and Houston and Garcia (1974). The horizontal (strike-slip) motion of the earthquake is neglected because of its low tsunami-generating capacity.

The time dependence of ground motions and the time scale t_c of the bed motion are important only in the case of ground motions of creeping type (Hammack, 1972), in which the time-size ratio

$$T = t_c(gh)^{1/2}/b_0\,, \tag{2}$$

is such that $T \gg 1$. In most large tsunamis, the ground motion is impulsive, i.e., $T \ll 1$ (Wilson and Torum, 1968; Hwang and Divoky, 1970). In the impulsive case, Hammack's (1972) results show that the actual time history of the bed motion is not of critical importance, and therefore the shape of the water surface at time $t = 0$, specified as initial values in numerical modeling, is the same as the ground displacement.

3. Numerical modeling

The finite difference model has been developed by Dean and Taylor (1971, 1972) and has been modified

[1] Present affiliation: School of Civil Engineering, Georgia Institute of Technology, Atlanta 30332.

0022-3670/82/020117-10$06.50

to include proper boundary and initial conditions for tsunami modeling. The unconditionally stable integration scheme is based on a four-level fractional step method (Yanenko, 1971; Richtmyer and Morton, 1967) with alternation of implicit and explicit techniques of solution. The difference equations are centered in both time and space coordinates, so that the errors introduced by discretization are only of second order in the space and time increments, Δx and Δt, respectively. The implicit part of the solutions to the tri-diagonal matrix equations are obtained through the double sweep method described by Abbott (1979) and Yanenko (1971). Details of the numerical model are given in the Appendix.

The model solves the depth-integrated, nonlinear equations of motion including the effects of earth's rotation and bottom friction. However, sensitivity runs of the model have shown that these effects are negligible within the spatial extent and the duration (16.7 h) used for modeling eastern Mediterranean tsunamis. Therefore, the nonlinear effects and the effects of bottom friction have been neglected. Earth's rotation has been included using an average value of the Coriolis parameter at 35° latitude, although its effects are expected to be small.

4. The eastern Mediterranean model

The bottom topography of the Levantine Basin is shown in Fig. 1. The mean depth of the basin is 2000–3000 m. The extension of the Crete–Rhodes arc in a southwesterly direction limits the connection to the other basins of the Mediterranean near the western end. To the east of this arc, depths of up to 4000 m exist, and by crossing the arc towards the Aegean Sea, the depth suddenly decreases to 500–1000 m. Narrow continental shelf regions surround the Levantine Basin except near the Nile Delta and the Gulf of Iskenderun, where the continental shelves are comparatively wider. The Cilician Basin, located between Turkey and Cyprus, is in the shape of a platform with a mean depth of 1000 m.

The modeled area (Fig. 2) has a size of 627 × 824 km. The tsunami source is located at the northwestern end near the Crete–Rhodes arc, centered at 27°44′E and 35°26′N. The rectangular source region has width b_0 = 125 km and length l_0 = 350 km (the difference of scales in the two horizontal directions in Fig. 2 makes the rectangular region appear as a parallelogram). The centerline (dashed lines) of the source region makes an angle of 45° from north. The

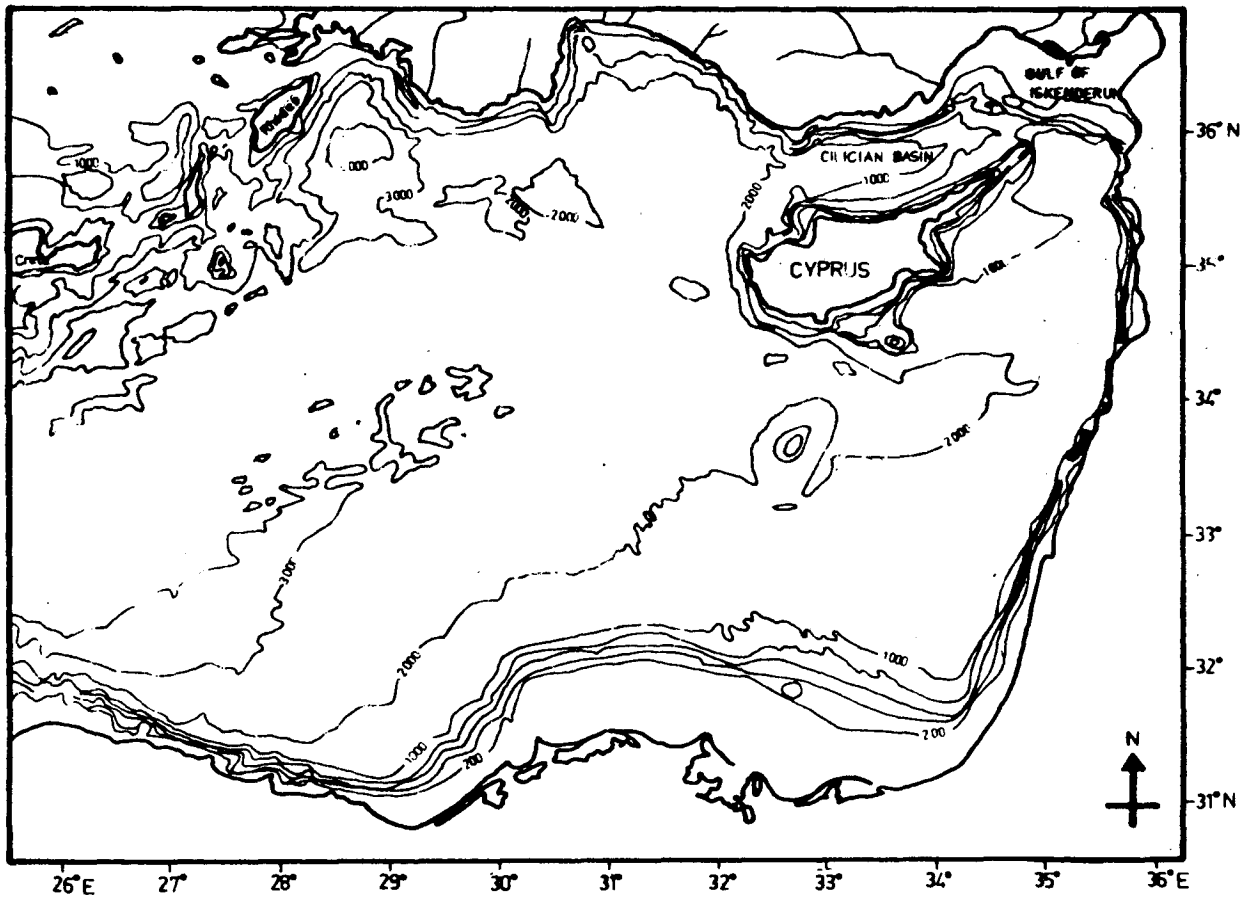

FIG. 1. Bottom topography of the eastern Mediterranean basin (depth in meters).

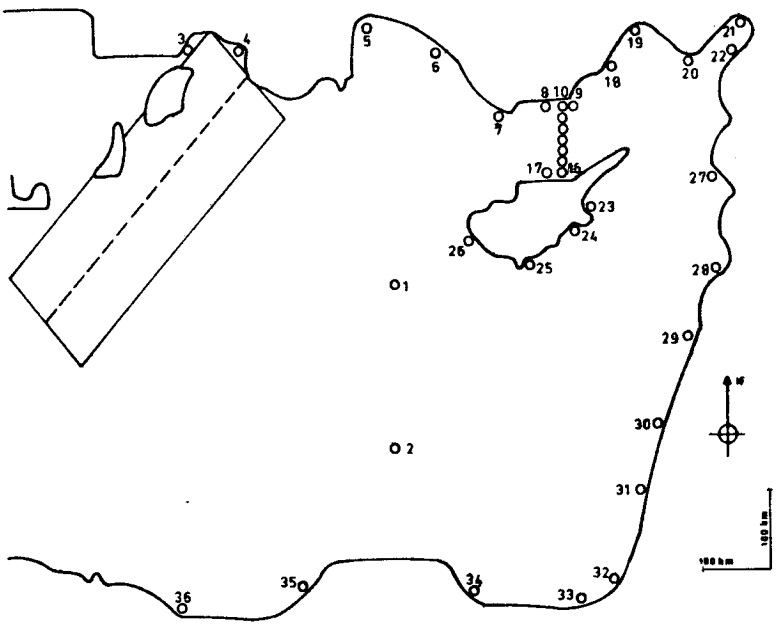

FIG. 2. The numerical modeling area, the tsunami source region and the stations selected for analyses.

source parameters selected correspond to a $M = 8$ (magnitude on Richter scale) earthquake with a return period of 10^4 years.

Three sides of the model area are closed and the normal velocity components along these coasts are set to zero as boundary conditions. The opening to the Aegean Sea is also closed in the model due to the sudden change in depth across the Cretan Arc region. Historical evidence of tsunamis (TSI, 1979) as well as modeling results suggest that disturbances in the Levantine Basin do not radiate into the Aegean region and vice versa. A simplified radiation boundary condition is applied at the western open boundary, i.e.,

$$\eta_t - (gh)^{1/2}\eta_x = 0, \qquad (3)$$

where η is the surface displacement, g the gravitational acceleration, h the depth, t the time, and x the distance towards west. This boundary condition requires that long waves reaching the western boundary propagate outwards from the modeling region.

The grid size used in the model is $\Delta x = 11$ km. The depth data is digitized from a 1:1 100 000-scale hydrographic map. The time increments used in the integration are $\Delta t = 100$ s and the integration is carried out for a total of 600 time steps.

In order to study the frequency response of the eastern Mediterranean to the tsunami excitation, time series of surface elevation at 36 stations (shown in Fig. 2) are frequency-analyzed.

a. Patterns of propagation

The propagation patterns of the tsunami wave are visualised by contouring the nodal lines at which the surface displacement changes sign. For example, the pattern at $t = 4000$ s is shown in Fig. 3a. The leading front of the wave motion and the leading crest are shown by broken lines. The region to the east of the wave front is undisturbed. The leading wave is slowed down at the shallower continental shelf regions and therefore the frontal line curves toward the coast. The effect of the Nile cone is seen to be most pronounced in delaying the leading wave. Following the first crest, a series of trailing waves are seen to propagate most of the wave energy toward the southeastern corner of the basin. The edge of this energy-radiation region extends from Crete to the Nile Delta. Very little energy is radiated outside this region and also towards the Aegean Sea. The sharp changes in depth at the Cretan arc region and the blocking effect of the islands cause almost total reflection and intensification of the energy radiated toward the southeastern corner of the basin.

The wave motion after 60 000 s is visualized in Fig. 3b. The waves are seen to have much shorter wavelengths as compared to Fig. 3a, due to the multiple reflections of the shorter waves from the coasts. Due to resonances within the system, trapping of waves occurs in certain regions. Such standing waves are seen at the Gulf of Iskenderun and to the east of the Nile delta.

b. Wave motions at selected stations

The time history of surface displacement at selected stations is shown in Fig. 4. This figure illustrates the frequency-selectivity and amplification as a result of local geometrical features.

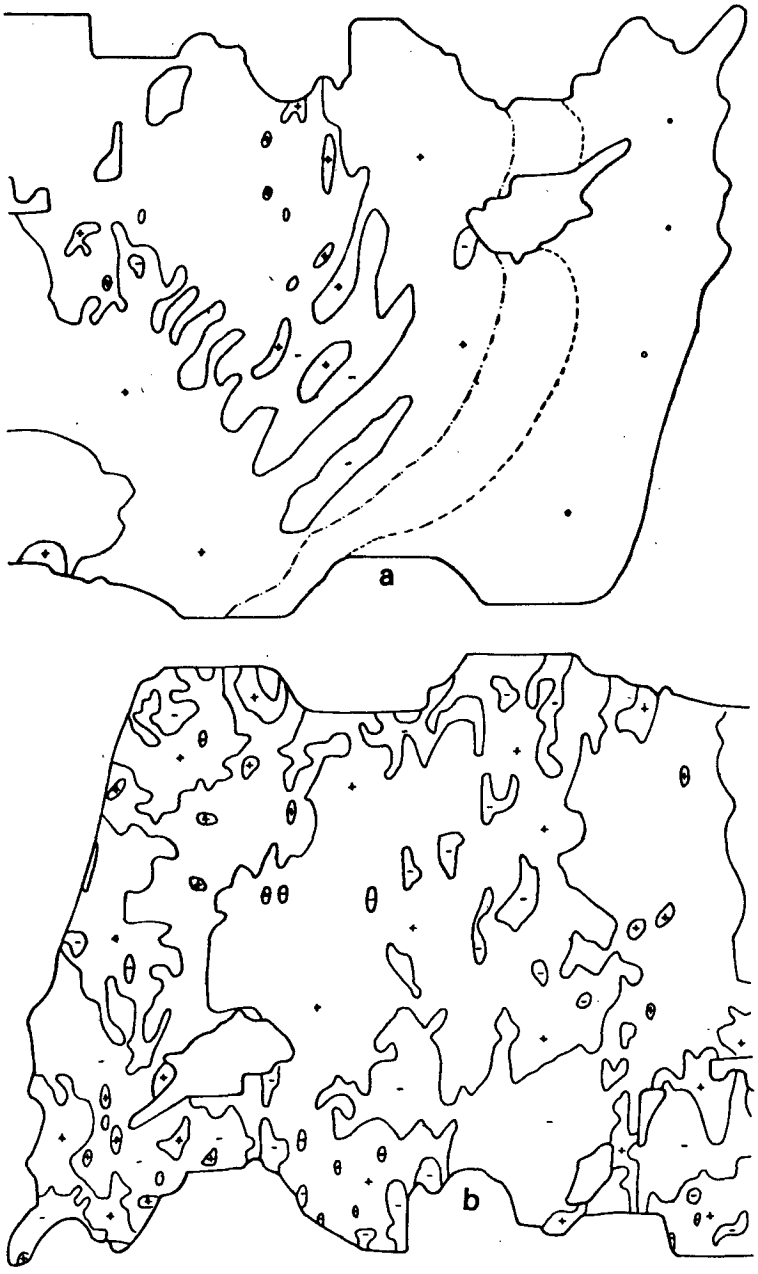

FIG. 3. The tsunami propagation pattern (a) at t = 4000 s and (b) at t = 60 000 s.

At the mid-basin station (station 2), a lead wave of 2 m height is identified, followed by a lower-amplitude trailing portion which becomes highly disorganized with increasing time. The coastal stations show a completely different behavior, in that the trailing waves at times can be larger than the initial lead wave and become organized and persistent at certain frequencies.

This general overview of the time histories shows that each coastal locality selects its own natural periods of oscillation from the rather disorganized motions at the central locations of the basin. The most organized (and hence selective) motions occur at the Gulf of Iskenderun and the Nile Delta regions.

The motions near the northeastern corner of the Levantine basin are of special interest, as will be explained further in the next section. Here, the wave motion becomes more organized as one moves from station 10 to station 19 and 21, respectively. The high-frequency motions at station 10 are replaced by higher amplitude, long-period motions near the eastern stations. Correspondingly, the continental

shelf near station 10 is narrow and becomes considerably wider near the Gulf of Iskenderun. These points will further be studied through frequency characteristics.

c. Frequency response

The time-series of water-surface displacement data generated by the model at all 36 stations are frequency-analyzed to detect and display the selective amplification characteristics of each locality. The Fourier amplitudes at each station are plotted against frequency in Fig. 5. The frequency axis has been terminated at 6 cph, since the oscillations with periods <600 s (10 min) are sufficiently small, and rather limited by the time increment used in the integration.

The amplitude spectra for the mid-basin stations 1 and 2 do not have any pronounced peaks. The energy is uniformly distributed with respect to frequency, since the initial disturbance also contains a wide band of frequency components due to the exponentially decaying ground displacement described earlier. As opposed to the mid-basin stations, coastal stations display prominent peaks at distinct frequencies and stations close to each other or within the same geometrical region usually have similar response curves. In principle it should be possible to explain the nature of such resonances by considering the geometry of each region, although each part of the basin may be coupled to other regions and the geometry is usually too complicated for simplification.

The stations on the southern coast of Cyprus, and on the coasts of Syria, Lebanon, Israel and Egypt are seen to have resonant peaks corresponding to their particular shelf geometries. Assuming a linearly varying shelf topography, natural periods of harmonic oscillations forced at the shelf break can be estimated from

$$T_n = l_1/[j_n(gh_1)^{1/2}], \quad n = 1, 2, \ldots, \qquad (4)$$

where n is the modal number for the oscillations, j_n the zeroes of the Bessel function J_0, l_1 the width of the shelf regions, and h_1 the depth at the shelf break. Alternatively, the natural periods of coastal-trapped edge waves (LeBlond and Mysak, 1978) excluding the effects of earth's rotation can be estimated by using Ursell's (1952) theory:

$$T_n = \left[\frac{2\pi\lambda}{g\sin(2n-1)\beta}\right]^{1/2}, \quad n = 1, 2, \ldots, \qquad (5)$$

where β is the inclination angle of the continental shelf topography and λ is the wavelength of the edge waves.

A comparison of peaks observed in numerical results and natural periods estimated from Eqs. (4) and (5) can be made. However, a certain caution is needed due to the uncertainties in determining the idealized dimensions of shelf topography and due to the relatively coarse resolution of the model in the shelf regions. In general, satisfactory results are obtained from the model, since narrow shelf regions such as near Beirut (29) and Lattakia (27) are excited at higher frequencies than those calculated for wide and shallow shelf regions such as near the Nile delta (32, 33, 34, 35) and near Mersin (19, 20, 21, 22). Natural periods estimated from Eqs. (4) and (5) for some of the stations are provided in Table 1. Periods of edge wave modes [Eq. (5)] are dependent on the wavelength of the incident wave, whereas the initial disturbance comprises an infinite number of wavelengths. A simple estimate of the initial wavenumber spectrum can be obtained from the initial surface displacement pattern along the minor axis of the generation regions [Eq. (1)]:

$$\tilde{\Delta}(k) = \frac{1}{b_0}\int_{-b_0/2}^{b_0/2} \Delta(x)e^{ikx}dx \approx \frac{\Delta_0}{6[(kb_0/12)^2+1]}, \qquad (6)$$

where $k = 2\pi/\lambda$ is the wavenumber. It is clear that the wavenumber spectrum is monotonically decreasing for increasing wavenumber, and most of the energy is confined to wavenumbers $k > 12/b_0$. Since

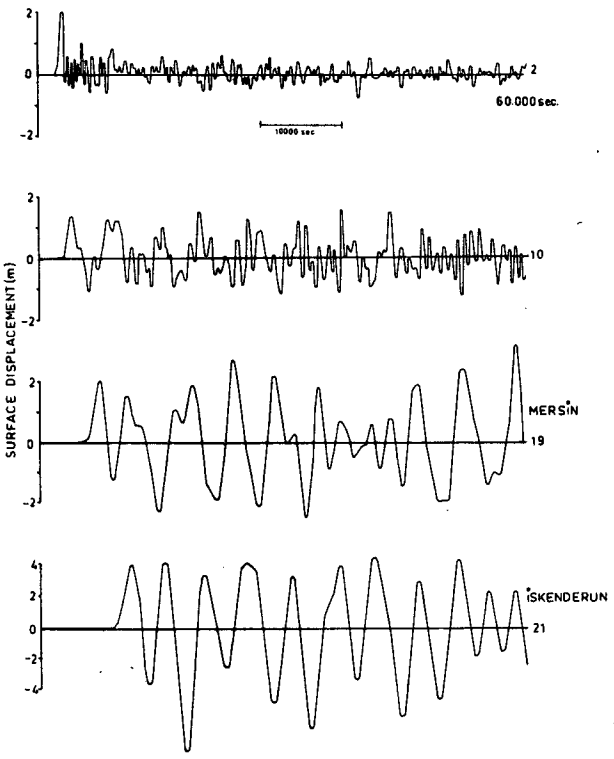

FIG. 4. Time histories of the tsunami wave at some eastern Mediterranean stations.

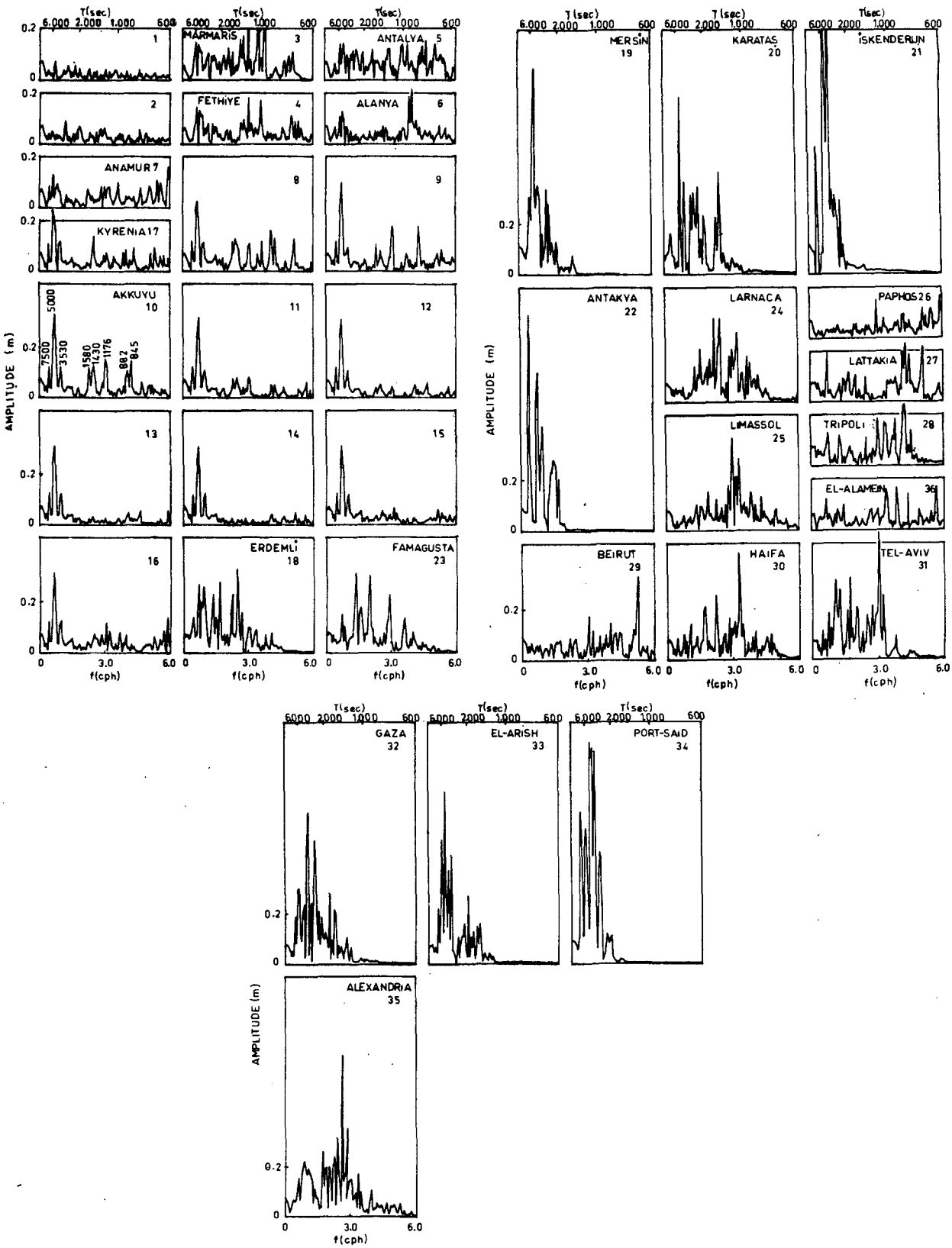

FIG. 5. Amplitude spectra of the wave motion at selected stations.

b_0 = 125 km, it can be estimated that most of the initial energy is given to wavelengths $\lambda \gtrsim 60$ km. The initial spreading of the energy in Fig. 3a also indicates that these wavelengths are dominant. Therefore calculations of edge wave periods from Eq. (5) presented in Table 1 are based on a wavelength of 60 km, but the actual periods can be larger than those given, depending on the actual wavelengths excited at the shelf regions.

On the Turkish coast, stations 3–7 located to the west of Anamur display few pronounced peaks. In comparison, stations 8–22 to the east of Anamur (within the Cilician Basin region) have remarkably more selective response curves. The region is affected by the general geometrical characteristics of the Cilician Basin. In order to study these oscillations in more detail, critical stations have been established on the coasts and on a transect across the Cilician Basin (stations 8–22).

At most stations in the area, three or more low-frequency peaks with periods >3000 s are consistently detected. Specifically, the peaks at 3530, 5000, and 7500 s observed at station 10 are present in most stations and become larger in size in Mersin (19) and within Iskenderun Bay (21).

Since a submarine sill extends from Cape Andreas, Cyprus to Iskenderun Bay on the Turkish coast (see Fig. 1), the Cilician Basin can be modeled as a rectangular body of water which is closed at the east end and open to the eastern Mediterranean waters at the western end. The natural periods of such a basin with surface displacement specified at the open end can be calculated from

$$T_{mn} = (gh)^{-1/2}\{[m/2W]^2 + [(2n-1)/4L]^2\}^{-1/2}, \quad (7)$$

where h is the depth, g the gravitational acceleration, W the width of the channel and L the length. m and n are the modal numbers in the cross-channel and lengthwise directions, respectively. If it is assumed that L = 150 km, W = 90 km and h = 1000 m for the Cilician Basin, the first mode along-channel oscillation period is calculated as T_{01} = 6000 s. Similarly, the natural periods of Iskenderun Bay can be calculated using Eq. (7), since it could also be modeled as a rectangular basin. Assuming L = 50 km, W = 40 km, and h = 70 m, the first-mode longitudinal oscillation period is T_{01} = 7560 s. Furthermore, a simple calculation for the continental shelf regions adjoining the Gulf of Iskenderun using Eq. (4) and assuming l_1 = 49.5 km and h = 200 m yields T_1 = 5800 s for the first mode of the continental shelf. These simple estimates show that the first mode oscillations of the Cilician Basin, Gulf of Iskenderun, and the continental shelf adjoining Iskenderun correspond to the low-frequency peaks in the amplitude spectra. The closeness of the triple peaks with periods >3000 s points to the significance of the coupled oscillations of the system. In summary, the Cilician Basin–Gulf of Iskenderun system can be idealized by the geometry shown in Fig. 6, as compared to the actual topography shown in Fig. 1.

TABLE 1. Calculated natural periods of shelf stations.

Station	l_1 (m)	h_1 (m)	β (deg)	Eq. (4) T_1 (s)	Eq. (4) T_2 (s)	Eq. (5) (λ = 60 km) T_1 (s)	Eq. (5) (λ = 60 km) T_2 (s)
Mersin	49500	200	0.23	5795	2519	3094	1786
Lattakia	5500	200	2.08	644	280	1029	595
Beirut	5500	200	2.08	644	280	1029	595
Tel-Aviv	19800	200	0.58	2318	1008	1948	1125
Gaza	22000	200	0.52	2576	1120	2058	1188
Port Said	60500	200	0.19	7083	3080	3404	1965
Alexandria	22000	200	0.52	2576	1120	2058	1188

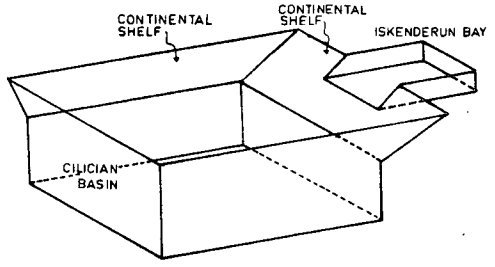

FIG. 6. Idealized geometry of the Cilician Basin–Gulf of Iskenderun Region.

In addition to the low-frequency peaks, the amplitude spectrum at station 10 displays peaks near 1500, 1200 and 850 s. These are higher modes of the Cilician Basin system and correspond to coupled oscillations of the shelf region along the Turkish coast and the deeper parts of the basin. At the 1500 and 850 s periods the splitting of the peaks corresponds to a beating oscillation due to the presence of coupling. The oscillations at these frequencies are seen to be larger on the shelf region (station 10) as compared to the oscillations in the deeper section (stations 11–16). An analogy can be made to a coupled mechanical system with two degrees of freedom if one of the oscillators within the system is assumed to have a much smaller mass than the other. Beating oscillations of this system are possible with the smaller mass absorbing most of the energy of the larger mass (Den Hartog, 1956).

In order to demonstrate the resonant excitation of the oscillations of 850 s period, the time series at station 10 has been band-passed filtered. The filter frequency response shown in Fig. 7a admits oscillations with periods between 800 and 900 s. The resulting band-passed time series shown in Fig. 7b displays an initial resonant growth after t = 20 000 s, and thereafter the oscillations are modulated with a beating period of 16 000 s. The beating period

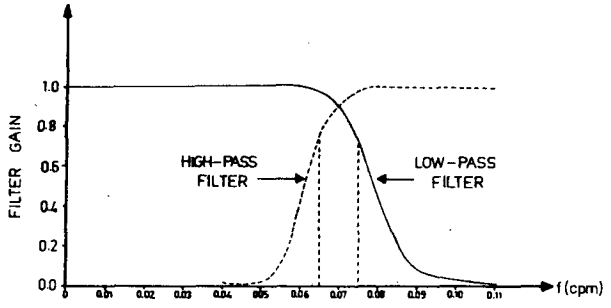

FIG. 7a. Band-pass filter function obtained by consecutive application of low-pass and high-pass filters.

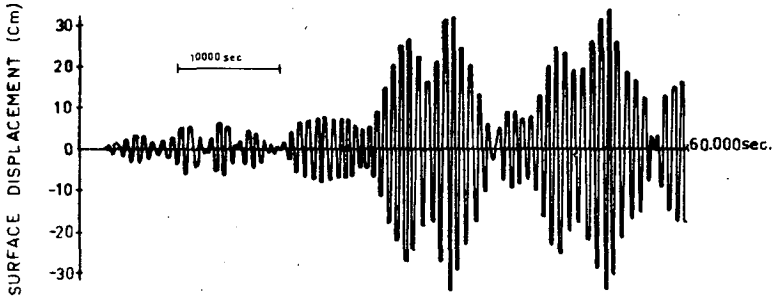

FIG. 7b. Band-pass filtered time series at station 10.

agrees with the period calculated from the frequency separation of the double peaks at 845 and 882 s periods, respectively. The modulation is a result of the surging of energy between different parts of the coupled system.

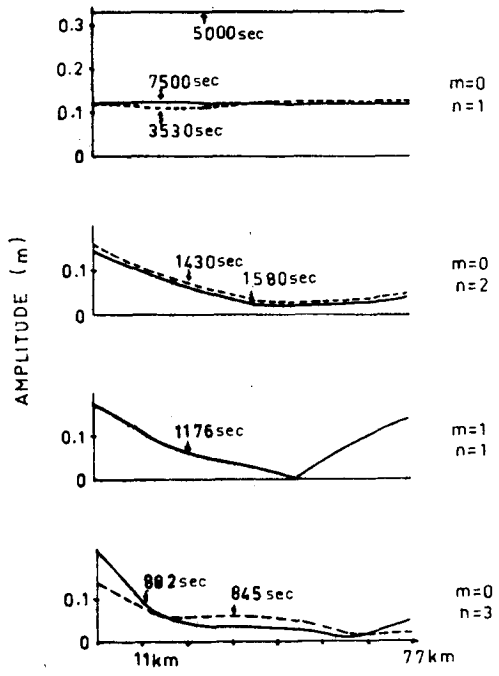

FIG. 8. The cross-channel modal amplitudes of tsunami waves in the Cilician Basin.

The cross-channel variations of the major peaks in amplitude spectra are shown in Fig. 8. Oscillations with periods >3000 s are seen to be uniform across the channel, since these modes correspond to the lengthwise oscillations in the Cilician Basin. Oscillations at 1500 and 850 s have a maximum amplitude on the Turkish continental shelf and they gradually decay towards Cyprus. The 1200 s waves have a nodal point at the middle of the channel, and correspond to the first mode of the cross-channel oscillations. The ordering of the modes shown in Fig. 8 has been guided by other numerical trial runs for a closed rectangular channel with a step-shaped continental shelf on one side.

5. Radiation losses

There is little evidence on how tsunamis of eastern Mediterranean origin propagate into the western Mediterranean, but historical records (Ambraseys, 1962) indicate that on certain occasions tsunamis originating near the Cretan island arc have been detected at low to moderate scales in the western basin, especially near the Adriatic Sea, Sicily and the southern Italian coast (e.g., tsunamis of 21 July 365, December 1303 and 20 September 1867). In the present study, a radiation boundary condition has been applied at the western boundary of the eastern Mediterranean region due to modeling considerations (Section 4). Therefore, a calculation of energy losses due to radiation is appropriate at this point.

The total energy (kinetic + potential) of the system at any time is given by

$$E = KE + PE = \rho \int_S \{\tfrac{1}{2}\mathbf{u}\cdot\mathbf{u} + \tfrac{1}{2}g\eta^2\}dS, \quad (8)$$

where ρ is density, $\mathbf{u}$ the velocity vector, η the surface displacement, and S the surface area of the modeled sea region. The initial potential energy of the disturbance is calculated as

$$E_0 = \tfrac{1}{2}\rho g \int_S \eta_0^2 dS = 1.14 \times 10^{15} \text{ J}. \quad (9)$$

The model run has been terminated at $t = 60\,000$ s, and the total energy of the system at this time is calculated as $E = 0.54 \times 10^{15}$ J (it is also observed that the energy is equipartitioned at this time with $KE = PE = 0.27 \times 10^{15}$ J). The ratio of the energy loss (to initial energy) and the mean energy dissipation rate due to radiation within the total duration of the model run is thus calculated to be 52.5% and 1.00×10^{10} J s^{-1}, respectively. The radiation of the tsunami waves into the western Mediterranean region accounts for a rather large loss compared to the initial earthquake energy input. The spreading of eastern Mediterranean tsunamis into the western Mediterranean, and possible multiple reflections within the confined waters of the Mediterranean basin, should be the subject of further study, and perhaps a more detailed model.

6. Conclusions

Numerical modeling techniques have been used to study the propagation of tsunami waves in the eastern Mediterranean. Detailed analyses of the results have indicated the possibilities of coupled resonances at the Cilician Basin region. The characteristics of these resonances have been explained and the regional responses have been obtained for a representative tsunami event in the eastern Mediterranean.

Acknowledgments. This research has been supported by the Turkish Electric Authority under Project code no. 77-07-00-06. The encouragement and approval of Dr. R. Bruce Taylor for adapting the numerical scheme to tsunami modeling is sincerely appreciated.

APPENDIX

The Numerical Model

The numerical model solves the following depth-integrated shallow-water hydrodynamical equations:

$$\frac{\partial q_x}{\partial t} + \frac{1}{D}\left\{2q_x\frac{\partial q_x}{\partial x} + q_y\frac{\partial q_x}{\partial y}\right\} + \left\{gD - \frac{q_x^2}{D^2}\right\}\frac{\partial \eta}{\partial x} - q_y\left\{f_0 + \frac{q_x}{D^2}\frac{\partial \eta}{\partial y}\right\} + \frac{q_x}{D}\frac{\partial q_y}{\partial y} + \frac{f q_x}{8D^2}|q| = 0, \quad \text{(A1a)}$$

$$\frac{\partial q_y}{\partial t} + \frac{1}{D}\left\{2q_y\frac{\partial q_y}{\partial x} + q_x\frac{\partial q_y}{\partial x}\right\} + \left\{gD - \frac{q_y^2}{D^2}\right\}\frac{\partial \eta}{\partial y} + q_x\left\{f_0 - \frac{q_y}{D^2}\frac{\partial \eta}{\partial x}\right\} + \frac{q_y}{D}\frac{\partial q_x}{\partial x} + \frac{f q_y}{8D^2}|q| = 0, \quad \text{(A1b)}$$

where g is the gravitational acceleration, f_0 the Coriolis parameter, f the Darcy-Weisbach friction coefficient, and D the stillwater depth. The depth-integrated volume fluxes are represented as

$$q_x = \int_{-D}^{\eta} u\,dz, \quad \text{(A2a)}$$

$$q_y = \int_{-D}^{\eta} v\,dz, \quad \text{(A2b)}$$

$$|q| = (q_x^2 + q_y^2)^{1/2}, \quad \text{(A2c)}$$

where u, v are the velocity components in the x, y directions respectively.

In order to develop an unconditionally stable scheme of integration, a four-level implicit/explicit alternating finite difference formulation is used. All coefficients and derivatives are centered in both space and time to render second-order accuracy, i.e., errors of only $O(\Delta t^2, \Delta x^2, \Delta y^2)$. To this end, the momentum and continuity equations are "falsified" in each fractional step to ensure that the composite equations over the four fractional steps are correctly centered difference equations. The equations are solved in the following sequence:

Fractional step	Equations solved	Method	Variables calculated
1. $t = (n + \frac{1}{4})\Delta t$	x-continuity x-momentum	explicit	$\eta^{n+1/4}$, $q_x^{n+1/2}$
2. $t = (n + \frac{1}{2})\Delta t$	y-continuity y-momentum	implicit	$\eta^{n+1/2}$, $q_y^{n+1/2}$
3. $t = (n + \frac{3}{4})\Delta t$	y-continuity y-momentum	explicit	$\eta^{n+3/4}$, q_y^{n+1}
4. $t = (n + 1)\Delta t$	x-continuity x-momentum	implicit	η^{n+1}, q_x^{n+1}

For the centering of differences in both time and space, the following modifications are made on some of the terms at fractional steps:

a. x-momentum equation

(i) The terms

$$\frac{q_y}{D}\frac{\partial q_y}{\partial y}, \quad -\frac{q_x q_y}{D^2}\frac{\partial \eta}{\partial y}, \quad \frac{q_x}{D}\frac{\partial q_y}{\partial y}$$

are omitted from the first fractional step and double-weighted in the fourth fractional step.

(ii) The term $2q_x/D\partial q_x/\partial x$ is eliminated by substitution from the continuity equation with which the particular x − momentum equation is coupled.

b. y-momentum equation

This is similar to (a) but applies to the second and third fractional steps.

c. Continuity equation

(i) In the first and fourth fractional steps, the term $\partial q_x/\partial x$ is double-weighted and $\partial q_y/\partial y$ is omitted.

(ii) In the second and third fractional steps, the term $\partial q_y/\partial y$ is double-weighted and $\partial q_x/\partial x$ is omitted.

REFERENCES

Abbott, M. B., 1979: *Computational Hydraulics.* Pitman, 324 pp.

Aslan, E., L. Tezuçan, and M. Bath, 1975: *An earthquake catalogue for Turkey for the interval 1913–1970.* Kandilli Observatory, Seismological Dept., Istanbul, 40 pp.

Ambraseys, N. N., 1962: Data for the investigation of the seismic sea-waves in the eastern Mediterranean. *Bull. Seismol. Soc. Amer.*, **52,** 895–911.

Benioff, H., 1964: Earthquake source mechanisms. *Science*, **143,** 1399–1406.

Dean, R. G., and R. B. Taylor, 1971: Numerical modeling of hydromechanics of Biscayne Bay, card sound system. Part I, nondispersive characteristics. Dept. Coastal and Oceanographic Engineering, University of Florida, 52 pp.

——, and ——, 1972: Numerical modeling of constituent transport in bay systems. *Proc. 13th. Coastal Engineering Conf.*, Vancouver, B.C., Amer. Soc. Civil Engineers, pp. 2227–2249.

Den Hartog, J. P., 1956: *Mechanical Vibrations.* McGraw-Hill.

Ergin, K., U. Güçlü and Z. Uz, 1967: A catalogue of earthquakes for Turkey and surrounding area. Fac. of Mining Eng., Technical University of Istanbul.

Hammack, J. L., 1972: Tsunamis–A model of their generation and propagation. Tech. Rep. KH-R-28, W. M. Keck Lab. Hydrol. Water Res., California Institute of Technology, 261 pp.

Houston, J. R., and A. W. Garcia, 1974: Type 16 flood insurance study: tsunami predictions for Pacific coastal communities. Tech. Rep. H-74-3, U.S.A.E., Waterways Exp. Sta.

Hwang, L. S., and D. Divoky, 1970: Tsunami generation. *J. Geophys. Res.* **75,** 6802–6817.

Karnik, V., 1969: *Seismicity of the European Area*, Part 1. D. Reidel, 364 pp.

——, 1971: *Seismicity of the European Area*, Part 2. D. Reidel, 218 pp.

LeBlond, P. H., and Mysak, L. A., 1978: *Waves in the Ocean.* Elsevier, 602 pp.

Momoi, T., 1962: Directivity of water waves generated by elliptic bottom source movements. *Bull. Earthquake Res. Inst.*, **40.**

Okamoto, S., A. Tabban and T. Tanuma, 1970: Earthquake intensity catalogue for Turkey. Earthquake Research Institute, Ankara, 122 pp.

Reid, H. P., 1910: The mechanics of the earthquake, the California earthquake of April 18, 1906. Report of the State Investigation Commission, Vol. 2, Carnegie Inst., Washington, DC.

Richtmyer, R. D., and K. W. Morton, 1967: Difference Methods for Initial Value Problems. *Interscience*, 405 pp.

TS1, 1979: Akkuyu nuclear power plant tsunami study. Inst. Marine Res., Middle East Technical University, 147 pp.

Ursell, F., 1952: Edge waves on a sloping beach. *Proc. Roy. Soc. London*, A214, 79–97.

Van Dorn, W. G., 1965: Tsunamis. *Advances in Hydroscience*, Vol. 2, Academic Press, 1–44.

Wilson, B. W., and A. Torum, 1968: Tsunami of the Alaskan earthquake, 1964; engineering evaluation. U.S. Army Corps Engineers, Coastal Eny. Res. Center, Tech. Memo, No. 25, 401 pp.

Yanenko, N. N., 1971: *The Method of Fractional Steps.* Springer-Verlag.